

09/20/2016

Tidally Induced Pulsations in Kepler Eclipsing Binary KIC 3230227

Zhao Guo, Douglas R. Gies

*Center for High Angular Resolution Astronomy and Department of Physics and Astronomy,
Georgia State University, P. O. Box 5060, Atlanta, GA 30302-5060, USA;
guo@astro.gsu.edu, gies@chara.gsu.edu*

Jim Fuller

*TAPIR, Walter Burke Institute for Theoretical Physics, Mailcode 350-17, Caltech,
Pasadena, CA 91125, USA;*

*Kavli Institute for Theoretical Physics, Kohn Hall, University of California, Santa
Barbara, CA 93106, USA;
jfuller@caltech.edu*

ABSTRACT

KIC 3230227 is a short period ($P \approx 7.0$ days) eclipsing binary with a very eccentric orbit ($e = 0.6$). From combined analysis of radial velocities and *Kepler* light curves, this system is found to be composed of two A-type stars, with masses of $M_1 = 1.84 \pm 0.18 M_\odot$, $M_2 = 1.73 \pm 0.17 M_\odot$ and radii of $R_1 = 2.01 \pm 0.09 R_\odot$, $R_2 = 1.68 \pm 0.08 R_\odot$ for the primary and secondary, respectively. In addition to an eclipse, the binary light curve shows a brightening and dimming near periastron, making this a somewhat rare eclipsing heartbeat star system. After removing the binary light curve model, more than ten pulsational frequencies are present in the Fourier spectrum of the residuals, and most of them are integer multiples of the orbital frequency. These pulsations are tidally driven, and both the amplitudes and phases are in agreement with predictions from linear tidal theory for $l = 2, m = -2$ prograde modes.

1. Introduction

Heartbeat stars (HBs), named after the resemblance between their light curves and an electrocardiogram, are binary or multiple systems with very eccentric orbits. The HBs

that have been studied in detail include a late B-type star (Maceroni et al. 2009), A or F-type stars (Handler et al. 2002; Welsh et al. 2011; Hambleton et al. 2013; 2016; Smullen & Kobulnicky 2015), and red giant stars (Beck et al. 2014). Recently, Shporer et al. (2016) presented spectroscopic orbits for 19 single-lined HBs. The *Kepler* eclipsing binary catalog (Kirk et al. 2016) contains over 150 of these stars with the flag ‘HB’. The distribution of eccentricity (e) and orbital period (P) for *Kepler* eclipsing binaries (EBs) and the 19 HBs is shown by Shporer et al. (2016), who note that the HBs occupy the upper envelope of the (P, e) diagram.

The distributions of orbital period and T_{eff} of over 150 HBs in *Kepler* EB catalog are shown in Figure 1. The effective temperatures are taken from Armstrong et al. (2014). The majority of HBs seem to have orbital period shorter than 30 days. Their range of effective temperatures ($\sim 5000 - 7500$ K) suggests that most of them are of spectral type earlier than G (mostly G, F, and A).

KIC 3230227 (HD181850, BD+38 3544; $K_p=9.002$, $\alpha_{2000}=19:20:27.0253$, $\delta_{2000}=+38:23:59.459$) is an eclipsing binary, first included in the *Kepler* EB catalog in Slawson et al. (2011) and Prsa et al. (2011). The original catalog listed the time of eclipse minimum and orbital period as $T_0 = 54958.702188$ (BJD-2,400,000) and $P = 14.094216$ days, respectively. Later, the period was found to be half of the original value ($P = 7.0471062$ days). Uytterhoeven et al. (2011) analyzed the *Kepler* light curves of ~ 750 A- and F-type stars. Among them, KIC 3230227 was classified as an eclipsing binary with γ Doradus pulsations. Thompson et al. (2012) studied light curves of 17 heartbeat stars, including KIC 3230227. Thanks to the special light curves of HBs, they derived orbital parameters including the orbital inclination (i), eccentricity (e), and argument of periastron (ω_p). Armstrong et al. (2014) derived the effective temperatures of $9341 \pm 350\text{K}$ and $7484 \pm 606\text{K}$ for the primary and secondary, respectively, by fitting the SED (Spectral Energy Distribution) to the observed magnitudes. Niemczura et al. (2015) made a detailed analysis of their high resolution spectra of KIC 3230227. Atmospheric parameters were inferred from Na D, H Balmer, and metal lines. They found $T_{\text{eff}} = 8150 \pm 220\text{K}$ (from the Na D lines and SED), $T_{\text{eff}} = 8200 \pm 100\text{K}$ (from Balmer and metal lines), $\log g = 3.9 \pm 0.1$ and $v \sin i = 50 \pm 4 \text{ km s}^{-1}$. They also obtained abundances for many individual elements (C, N, O, Ne, Na, Mg, etc), as listed in their Table 4. Most of these abundances are close to solar values (Asplund et al. 2009; Lodders et al. 2009). We summarize the aforementioned results in Table 1.

2. Binary Modeling

The orbital parameters of KIC 3230227 were derived from radial velocity (RV) measurements in Smullen & Kobulnicky (2015). This system was found to be composed of two A-type stars with similar masses (mass ratio $q = 0.95 \pm 0.05$), and a very eccentric orbit ($e = 0.60 \pm 0.04$, $\omega_p = 293 \pm 4^\circ$). These orbital elements are also listed in Table 1.

Four orbital elements (P , i , e , and ω_p) were derived from the light curve alone in Thompson et al. (2012). It is important to note that the Kumar light curve model (Kumar et al. 1995) adopted in Thompson et al.’s work does not take into account the effects of reflection and eclipses. The orbital parameters derived by fitting the light curve with the Kumar model can be treated as good estimates, but they can also be off by a large margin, especially the orbital inclination if the reflection effect is important and/or eclipses occur.

A better treatment of the light curve modeling of HBs was performed for the face-on system KOI-54 by Welsh et al. (2011). These authors modeled the light curve and radial velocity curve simultaneously, taking advantage of their binary modeling tool ELC (Orosz & Hauschildt 2000). Stellar distortions were fully modeled with the Roche equipotential, and the reflection effect from mutual heating, plus the limb and gravity darkening effects are included. To synthesize the binary light curve, NextGen atmosphere models are used to integrate numerically the flux from the stellar surface. Several techniques are adopted in ELC to improve the integration accuracy, for example, Monte Carlo sampling on the fractional pixels at the eclipse horizon with Sobol sequences. Here we use the same tool to model KIC 3230227.

The *Kepler* SAP light curves were retrieved from MAST. There are 18 quarters (Q) of long cadence data (Q0-17). Short cadence light curves are only available from quarters 1, 2, and 5. We de-trended the raw light curve in each quarter following the procedure detailed in Guo et al. (2016). In short, the procedures include spline fitting to the long term trends, median difference corrections, outlier removal, and normalization. The de-trended light curves were then divided into six temporal sections and light curve modeling was performed for each section individually.

Obvious oscillations stand out in the light curves, and they are still present in the phase-folded light curves (Figure 2, 4). Their amplitudes are low enough to be treated as perturbations to the binary light curve. We adopted the period in the *Kepler* Eclipsing Binary Catalog ($P = 7.0471062 \pm 0.0000175$ days), which is based on the analysis of light curve by using the Lomb-Scargle periodogram and *kephem* software (Hambleton et al. 2013).

This system only shows a single, very narrow eclipse ($\Delta\phi \approx 0.02$ in phase) near periastron. In order to model fully the shape of the eclipse, we have to use a very small increment

in phase ($\delta\phi = 0.00055 = 0.2^\circ$). This makes the light curve computation relatively expensive. Aperture contamination parameters k listed in Kepler Input Catalog (KIC), which are the percent of contamination light from other stars in the photometric aperture, range from 0.08% to 0.2%. In ELC, this effect is corrected by adding to the median value of the model light curve y_{med} an offset $ky_{\text{med}}/(1 - k)$. In practice, this effect is usually very small and negligible (Hambleton et al. 2016) and we found no significant differences neglecting this effect. Based on the effective temperatures listed in Table 1, the two components are likely to have radiative envelopes, thus the gravitational darkening coefficients β_1 and β_2 are set to 0.25, and bolometric albedos l_1, l_2 are fixed to 1.0.

The rotational axis of the star is assumed to be aligned with the orbital angular momentum. We assume pseudo-synchronous rotation, which suggests the rotational frequency satisfies $f_{\text{rot}} = (1 + 7.5e^2 + 5.625e^4 + 0.3125e^6)/[(1 + 3e^2 + 0.375e^4)(1 - e^2)^{1.5}]f_{\text{orb}}$ (Hut 1981) ($f_{\text{rot}} = 4.08f_{\text{orb}}$ for $e = 0.6$). We use the orbital eccentricity $e = 0.60$ and argument of periastron $\omega_p = 293^\circ$ from Smullen & Kobulnicky (2015) as initial values. The mass ratio q and primary semi-amplitude velocity K_1 , taken from the same paper, are initially fixed to 0.95 and 98.5 km s⁻¹, respectively. It is well known that the light curves of eclipsing binaries are sensitive to the temperature ratio rather than individual temperatures. Thus the effective temperature of the primary T_{eff1} is fixed to 8000K, in agreement with the spectroscopic results in Table 1. We fit the light curve by optimizing the following parameters: e , ω_p , i , relative radius $r_1 = R_1/a$ and $r_2 = R_2/a$, time of periastron passage T , and effective temperature of the secondary T_{eff2} . The search for the χ^2 minimum was performed with the genetic algorithm *pikaia* (Charbonneau 1995), followed by a local search with the downhill simplex algorithm *amoeba*. Since ELC does not model pulsations in the light curve, the standard way of estimating uncertainties by finding the range of parameters that increases χ^2 by 1.0 from χ_{min}^2 cannot be used. Instead, we adopted the standard deviations of the best-fitting parameters in the six data sets as the 1σ errors. This is the method used by Guo et al. (2016), and it can account for possible systematic uncertainties due to light curve de-trending.

The final optimized solution has essentially the same e and ω_p values as those in the RV work of Smullen & Kobulnicky (2015). The orbital inclination ($i = 73.42^\circ$), however, is much larger than the result in Thompson et al. (2012) ($i = 43^\circ$), and close to that in Smullen & Kobulnicky (2015) ($i \sim 66^\circ - 71^\circ$). As shown in Figure 2, our light curve model matches the observations down to the level of 0.001 magnitude. The profile of the narrow eclipse is also well modeled. The secondary has a slightly higher effective temperature $T_{\text{eff2}} = 8177\text{K}$ and smaller mass and radius ($M_2 = 1.73M_\odot$, $R_2 = 1.68R_\odot$), compared to that of the primary ($T_{\text{eff2}} = 8000\text{K}$, $M_1 = 1.84M_\odot$, $R_1 = 2.01R_\odot$). The main parameters of our ELC model are listed in Table 2. The projected rotational velocities ($v \sin i_1 = 56.4$ km

s^{-1} , $v \sin i_2 = 47.0 \text{ km s}^{-1}$), under the assumption of pseudo-synchronous rotation, are in approximate agreement with the measured $v \sin i$ from spectra as listed in Table 1. We found that the best-fit light curve solution from one data set or quarter can almost match the light curve of other quarters equally well. In terms of argument of periastron ω_p , no discernable apsidal motion was found.

The flux-weighted radial velocity curves from our ELC model are shown in Figure 3, matching the original RV measurements in Smullen & Kobulnicky (2015) very well. In the right two panels, we also show the predicted Rossiter-McLaughlin effect during the eclipse. It can be seen that in order to measure this effect, a RV precision better than 0.5 km s^{-1} is needed.

3. Pulsation Characteristics

3.1. Tidally Induced Pulsations

To study the pulsations, we obtained the residuals by subtracting the best binary light curve model from the observations. Figure 4 illustrates the pulsational light curve in Q14, together with the original binary light curve in Q14 and the short cadence light curve in Q5. We then calculated the Fourier spectrum by using the *Period04* package (Lenz & Breger 2005). A standard pre-whitening procedure was performed for the spectrum in each quarter. The fitting formula used is $Z + \sum_i A_i \sin(2\pi(f_i t + \delta_i))$, where Z , A_i , f_i , δ_i are the zero-point shift, amplitudes of pulsations, frequencies, and phases, respectively. The time t is with respect to the periastron passage: $t = \text{BJD} - 2,454,958.791621$. The calculation was performed to the long Nyquist frequency (24.47 d^{-1}). A similar calculation was performed with the short cadence residuals as well, but no peaks were found beyond the frequency $\approx 10 \text{ d}^{-1}$ in the spectrum. The strong pulsational frequencies are actually all below 5 d^{-1} .

The amplitude spectrum calculated from residuals of quarter 1 only and from quarters 0 – 17 are shown in Figure 5. The dominant feature in the spectrum is the equal spacing of the frequency peaks. The main pulsational frequencies and their amplitudes and phases are listed in Table 3. The uncertainties are calculated following Kallinger et al. (2008). We have labeled them as f_1 to f_{10} , in the order of increasing frequency. A close examination reveals that most of these peaks are exact integer multiples of orbital frequency ($f_{\text{orb}} = 1/7.0471062 = 0.141902 \text{ d}^{-1}$), for instance, f_3 , f_5 , f_6 , f_7 , f_8 , f_9 , and f_{10} . The orbital harmonic nature of the pulsational frequencies, together with the high eccentricity of the binary and the masses of the stars strongly suggest that these are tidally induced pulsations. Note that the two non-orbital-harmonic frequencies f_1 , f_2 can be added together to obtain an orbital

harmonic ($f_1 + f_2 = 9.88f_{orb} + 12.12f_{orb} = 22f_{orb}$). The same phenomenon was also found in the tidal oscillations frequencies of KOI-54. This can be explained by non-linear mode coupling as detailed by Burkart et al. (2012), O’Leary & Burkart (2014), and Weinberg et al. (2013). It is also interesting to note that $f_1 = 9.88f_{orb}$ and $f_4 = 13.88f_{orb}$ have the same fraction to the nearest orbital harmonic. The feature that nonharmonic frequencies share the common fractional parts in units of orbital frequency was discussed in detail by O’Leary & Burkart (2014) for KOI-54. This further supports the interpretation of these frequencies as the result of non-linear mode coupling.

Many frequency triplets can be seen in the spectrum, with equal spacing of orbital frequency. Close examination reveals that all these triplets have frequencies that are equal to $N - 0.12$, N , $N + 0.12$ times orbital frequency. Thus they can be explained as a combination of one real oscillation peak and two side-lobes due to the spectral window (Figure 5). The nonharmonic peaks f_1, f_2, f_4 generate side-lobes at $(N - 0.12)f_{orb}$ and $(N + 0.12)f_{orb}$. We find that after pre-whitening f_1, f_2 , and f_4 , these triplets essentially disappear, and only Nf_{orb} peaks remain, supporting the above argument. Low amplitude $m = 0$ modes can also exist. At high inclination, these modes are expected to have low amplitudes. As discussed below, the Ledoux constant C_{nl} (Ledoux 1951) is about 0.16 for the g -modes in the observed frequency range. This means the splitting δf is about $m(1 - 0.16)f_{rot}$ for modes with frequencies much higher than f_{rot} . If we adopt pseudo-synchronous rotation $f_{rot} = 4.1f_{orb} = 0.58 \text{ d}^{-1}$, δf are then 0.49 and 0.98 d^{-1} for $m = 1$ and $m = 2$, respectively. Thus the splittings will be located at several orbital harmonics away from their central $m = 0$ peak. This also suggests that the splittings are not due to rotation.

The amplitude variations of these oscillations are shown in Figure 6 and listed in Table 4. Most of the frequencies have relatively stable amplitudes over 16 quarters, with variations less than 0.05 milli-mag. The exception seems to be f_3 , which decreased from 0.174 milli-mag in Q1 to 0.078 milli-mag in Q16.

3.2. Mode Identification from Phases

Phases of tidal oscillations contain important information on the mode properties. O’Leary & Burkart (2014) identified the two dominant pulsations in KOI-54 as $l = 2, m = 0$ modes by studying their phases. Following their treatment, for standing modes, the phases of observed flux variation ($\delta J/J$) due to tidal oscillations that have N times the orbital frequency are:

$$\delta = \arg(\delta J_N / J_N) = \arg(A_{nlmN}) + \arg(Y_{lm}(\theta_0, \phi_0)) = \psi_{nlmN} + m\phi_0 \quad (1)$$

where, A_{nlmN} is the mode amplitude for the N th orbital harmonic (eq. 7 in Burkart et al. 2012) and (θ_0, ϕ_0) are observer's coordinates.

Since we express the pulsations with the formula $\sin(2\pi(f_it + \delta_i))$ instead of cosine functions, the observed phases (δ) in units of 2π are then :

$$\delta = \left(\frac{1}{4} + \psi_{nlmN} + m\phi_0 \right) \mod \frac{1}{2} \quad (2)$$

and

$$\phi_0 = \frac{1}{4} - \frac{\omega_p}{2\pi} \quad (3)$$

where $\omega_p = 293^\circ = 5.114$ rad is the argument of periastron from the RV and light curve analysis. In the limit of poor tuning, that is, the difference between intrinsic mode frequency of free oscillations and the nearest orbital harmonics ($\delta\omega = \omega_{nl} - N\Omega_{orb}$) is much larger than mode damping rate (γ_{nl}), $|\delta\omega| \gg \gamma_{nl}$, we have the following approximation,

$$\psi_{nlmN} \approx \left[\pi/2 - \arctan \left(\frac{\delta\omega}{\gamma_{nl}} \right) \right] / (2\pi) = [\pi/2 - \pi/2] / (2\pi) = 0 \quad (4)$$

The observed phase is then

$$\delta = \left(\frac{1}{4} + m\phi_0 \right) \mod \frac{1}{2} \quad (5)$$

Note that if using the magnitude variation, the phase will be off by π (by $1/2$ if in units of 2π), since $\delta\text{mag} \propto -\delta J/J$. In Figure 7, we show the observed phases of main oscillations. Within uncertainties, phases of $f_2, f_3, f_5, f_6, f_7, f_8, f_9, f_{10}$ can be explained by the theoretical phases of $l = 2, m = -2$ modes ($\delta_{m=-2} = 0.38, 0.88$). The phase of f_4 is close to the predicted phase of $m = 2$ modes ($\delta_{m=2} = 0.12$). Thus most of the observed oscillations are likely due to $l = 2, m = -2$ modes, in agreement with the expectations for the high inclination angle of the binary ($i = 73^\circ.4$). On the other hand, $l = 2, m = 0$ modes are expected to have low amplitudes, and none of the main frequencies have phases close to those predicted phases ($\delta_{m=0} = 0.25, 0.75$). We do not have strong evidence that the oscillations are in resonance locking, because amplitudes of resonance-locked modes are much larger than normal tidal oscillations (see the amplitude modeling below).

3.3. Theoretical Flux Variations

We want to study whether the observed amplitudes of tidal oscillations agree with theory. To this end, we evolve a star of $M = 1.84M_\odot$ with solar metallicity with MESA evolution code (Paxton et al. 2011, 2013) until its properties match the observations of the primary. The closest equilibrium model has the same radius ($R = 2.01R_\odot$), but slightly cooler effective temperature ($T_{\text{eff}}(\text{model}) = 7800\text{K}$ vs. $T_{\text{eff}}(\text{observation}) = 8000\text{K}$). We use parameters of the secondary ($M_2 = 1.73M_\odot$) for the calculation of tidal forcing from the companion.

Following Fuller & Lai (2012), the Lagrangian tidal displacement $\boldsymbol{\xi}(\mathbf{r}, t)$ can be expressed as the sum of displacement of free oscillations $\boldsymbol{\xi}_\alpha(\mathbf{r})$,

$$\boldsymbol{\xi}(\mathbf{r}, t) = \sum_{\alpha} c_{\alpha}(t) \boldsymbol{\xi}_{\alpha}(\mathbf{r}) \quad (6)$$

where α represents the mode indices which include (n, l, m) . The amplitude of each mode c_{α} is derived from solving the forced harmonic oscillator equation (their eq. 22), and the solution is given by their eq. 23. The expression of $c_{\alpha}(t)$ involves the sum over the forcing from each orbital harmonic N , and this is from the Fourier expansion of orbital motion in the eccentric orbit (their eq. 20). The displacement $\boldsymbol{\xi}_{\alpha}$ and various other eigenfunctions of $l = 2, m = 0$ modes are calculated with the GYRE code (Townsend & Teitler 2013) in the non-adiabatic mode. We use the updated collocation method COLLOC_GL2 to solve the oscillation equations which has better performance than the Magnus solver for non-adiabatic calculations.

We use the perturbative approximation which is valid when (angular) rotation frequency Ω_{rot} is much smaller than mode frequency (co-rotating frame) in the zero-rotation limit (ω_{nl}). The frequencies of $l = 2, m = -2$ prograde modes are calculated from $\omega_{\alpha} = \omega_{nlm} = \omega_{nl} + mC_{nl}\Omega_{\text{rot}}$. The mode eigenfunctions are normalized to have unit mode inertia and assumed to be unchanged by rotation.

Following Buta & Smith (1979), the magnitude variation of a single oscillation mode due to temperature changes has the following expression assuming pulsations are adiabatic:

$$\begin{aligned} & (\Delta \text{mag})_T \\ &= -1.0857 \frac{xe^x}{e^x - 1} \left[\frac{\xi_r(R)}{R} \frac{\Gamma_2 - 1}{\Gamma_2} \left(\frac{l(l+1)}{\omega^2} - 4 - \omega^2 \right) \right] \gamma_l \sqrt{\frac{(2l+1)(l-m)!}{4\pi(l+m)!}} P_l^m(\cos i_s) e^{im\phi_0} e^{i\omega_{\alpha}t} \end{aligned} \quad (7)$$

where $\xi_r(R)$ is the radial displacement evaluated at the stellar surface. The term in the square bracket $[\]$ is the approximation to the temperature perturbation at the stellar surface $\frac{\delta T}{T}|_R$, and $\frac{x e^x}{e^x - 1}$ arises from the blackbody approximation to the stellar atmosphere, with $x = hc/\lambda kT$. i_s is the orbital inclination, $\Gamma_2 \approx 5/3$ is the adiabatic index, and ω is the dimensionless mode frequency given by $\omega = \omega_\alpha/\sqrt{GM/R^3}$. γ_l is bolometric limb darkening coefficient defined in eq. (39) of Buta & Smith (1979). For an A-star similar to KIC 3230227, γ_l is about 0.3 in the *Kepler* passband. The above equation is good for the first-order approximation of magnitude variations, and a better treatment should fully take into account the non-adiabaticity of oscillations (J. Fuller 2016, in prep.). The variations due to geometric changes are usually much smaller and thus are not considered here.

Using eq. (7) and summing up the contribution from each mode α , we calculated the magnitude variation for each orbital harmonic N for $l = 2, m = -2$ prograde modes. The variations due to the equilibrium tide (setting $N\Omega_{\text{orb}} = 0$) have been subtracted. The result is shown in Figure 8, together with the observed amplitudes of oscillations. The predicted mode amplitudes are very sensitive to the mode detuning parameter $\delta\omega = \omega_\alpha - N\Omega_{\text{orb}}$, i.e., the difference between the intrinsic mode frequency ω_α and driving frequency $N\Omega_{\text{orb}}$. There is a strong peak at $N = 23$, which is due to a chance resonance (very small $\delta\omega$) for the stellar model that we use. A stellar equilibrium model with almost the same observed parameters (radius, temperature, and mass) and slightly different mode frequencies will have quite different mode detuning. Detailed amplitude modeling requires very fine grids of structure models and is beyond the scope of this paper (see Burkart et al. 2012). But overall, the theoretical predicted mode amplitudes seem to agree with observations. It further supports the argument that the oscillations are due to tidally excited $m = -2$ quadruple modes.

4. Summary and Future Prospects

The unprecedented light curves from the *Kepler* satellite offer us opportunities to study the effect of tides on stellar oscillations. Heartbeat stars in eclipsing systems are among the best laboratories since the model independent fundamental stellar parameters such as mass and radius can be determined. We presented a study of KIC 3230227, which consists of two A-type stars in an eccentric orbit with a period of 7 days. The observed pulsations, mostly orbital harmonics, can be explained by the tidally induced $l = 2, m = -2$ prograde modes. This is supported by a comparison of their observed and modeled phases and amplitudes.

The fundamental parameters of KIC 3230227 are determined only to 10% in mass and 5% in radius. Further analysis could take advantage of the high resolving power spectra and

more phase coverage in the RV curve. This is already underway (K. Hambleton, private communication). Once more accurate parameters are determined, asteroseismic modeling of these tidal oscillations can be performed, as was done in Burkart et al. (2012). To solidify the result of this work, mode identification techniques can be applied to the line profiles variations as well as to the time series of multi-color photometry. It is also worthwhile studying the Fourier spectrum more closely, identifying individual modes, and analyzing the non-linear mode couplings. Another weakness of this work is that we are unable to tell which star is pulsating. A study of pulsations during eclipse may help to clarify this issue (Bíró & Nuspl 2011).

We thank Jerome A. Orosz for making his ELC code available to us. We thank Bill Paxton, Rich Townsend and others for maintaining and updating MESA and GYRE. G. Z. is grateful to Joshua Burkart for explaining tidal asteroseismology, to Rachel Smullen for her help in clarifying some issues in the analysis of radial velocities. We thank Kelly Hambleton for useful discussions. This work is partly based on data from the *Kepler* mission. *Kepler* was competitively selected as the tenth Discovery mission. Funding for this mission is provided by NASA’s Science Mission Directorate. The photometric data were obtained from the Mikulski Archive for Space Telescopes (MAST). STScI is operated by the Association of Universities for Research in Astronomy, Inc., under NASA contract NAS5-26555. This study was supported by NASA grants NNX12AC81G, NNX13AC21G, and NNX13AC20G. This material is based upon work supported by the National Science Foundation under Grant No. AST-1411654. Institutional support has been provided from the GSU College of Arts and Sciences and the Research Program Enhancement fund of the Board of Regents of the University System of Georgia, administered through the GSU Office of the Vice President for Research and Economic Development.

REFERENCES

- Armstrong, D. J., Gomez Maqueo Chew, Y., Faedi, F., & Pollacco, D. 2014, MNRAS, 437, 3473
- Asplund, M., Grevesse, N., Sauval, A. J., & Scott, P. 2009, ARA&A, 47, 481
- Beck, P. G., Hambleton, K., Vos, J., et al. 2014, A&A, 564, A36
- Bíró, I. B., & Nuspl, J. 2011, MNRAS, 416, 1601
- Burkart, J., Quataert, E., Arras, P., & Weinberg, N. N. 2012, MNRAS, 421, 983
- Buta, R. J., & Smith, M. A. 1979, ApJ, 232, 213
- Charbonneau, P. 1995, ApJS, 101, 309
- Fuller, J., & Lai, D. 2012, MNRAS, 420, 3126
- Guo, Z., Gies, D. R., Matson, R. A., & García Hernández, A. 2016, ApJ, 826, 69
- Hambleton, K. M., Kurtz, D. W., Prša, A., et al. 2013, MNRAS, 434, 925
- Hambleton, K. M., Kurtz, D. W., Prša, A., et al. 2016, MNRAS, in press
- Handler, G., Balona, L. A., Shobbrook, R. R., et al. 2002, MNRAS, 333, 262
- Hut, P. 1981, A&A, 99, 126
- Kallinger, T., Reegen, P., & Weiss, W. W. 2008, A&A, 481, 571
- Kirk, B., Conroy, K., Prša, A., et al. 2016, AJ, 151, 68
- Kumar, P., Ao, C. O., & Quataert, E. J. 1995, ApJ, 449, 294
- Ledoux, P. 1951, ApJ, 114, 373
- Lenz, P., & Breger, M. 2005, Communications in Asteroseismology, 146, 53
- Lodders, K., Palme, H., & Gail, H.-P. 2009, in Landolt Börnstein Group VI Astronomy and Astrophysics, 4B, ed. J. E. Trümper (Berlin: Springer-Verlag), 34
- Maceroni, C., Montalbán, J., Michel, E., et al. 2009, A&A, 508, 1375
- Niemczura, E., Murphy, S. J., Smalley, B., et al. 2015, MNRAS, 450, 2764
- O’Leary, R. M., & Burkart, J. 2014, MNRAS, 440, 3036

- Orosz, J. A., & Hauschildt, P. H. 2000, *A&A*, 364, 265
- Paxton, B., Bildsten, L., Dotter, A., et al. 2011, *ApJS*, 192, 3
- Paxton, B., Cantiello, M., Arras, P., et al. 2013, *ApJS*, 208, 4
- Prša, A., Batalha, N., Slawson, R. W., et al. 2011, *AJ*, 141, 83
- Shporer, A., Fuller, J., Isaacson, H., et al. 2016, *arXiv:1606.02723*
- Slawson, R. W., Prša, A., Welsh, W. F., et al. 2011, *AJ*, 142, 160
- Smullen, R. A., & Kobulnicky, H. A. 2015, *ApJ*, 808, 166
- Thompson, S. E., Everett, M., Mullally, F., et al. 2012, *ApJ*, 753, 86
- Townsend, R. H. D., & Teitler, S. A. 2013, *MNRAS*, 435, 3406
- Uytterhoeven, K., Moya, A., Grigahcène, A., et al. 2011, *A&A*, 534, A125
- Weinberg, N. N., Arras, P., & Burkart, J. 2013, *ApJ*, 769, 121
- Welsh, W. F., Orosz, J. A., Aerts, C., et al. 2011, *ApJS*, 197, 4

Table 1. Atmospheric and Orbital Parameters

Parameter	Uytterhoeven et al. (2011)	Thompson et al. (2012)	Armstrong et al. (2014)	Smullen & Kobulnicky (2015)	Niemczura et al. (2015)
T_{eff} (K)	7970(290)	8750	9341(350) ^a , 7484(606) ^a	~ 8000	8150(220), 8200(100)
$\log g$ (cgs)	3.9 ± 0.3	5.0	—	4.0, 3.5	3.9(0.1)
$v \sin i$ (km s ⁻¹) ..	—	—	—	$\sim 30, \sim 75$	50(4)
[Fe/H]	—	—	—	≥ 0	≈ 0
P (days)	7.0471062(175) ^b	7.04711(87)	—	7.051(1)	
T_0 (BJD-2400000)	54958.702238 ^c	—	—	—	
T (BJD-2400000)	—	—	—	56311.76(03) ^d	
i (°)	—	42.79 ± 0.46	—	66 – 71	—
e	—	0.588(4)	—	0.60(4)	
ω_p (°)	—	292.1(1.2)	—	293(4)	
K_1 (km s ⁻¹)	—	—	—	98.5(5.4)	—
K_2 (km s ⁻¹)	—	—	—	104.9(6.1)	—
γ (km s ⁻¹)	—	—	—	-15.7(1.7)	—

^aFor the primary and secondary, respectively

^bKepler Eclipsing Binary Catalog

^cTime of eclipse minimum from Kepler Eclipsing Binary Catalog

^dTime of periastron passage

Table 2. Model Parameters

Parameter	Primary	Secondary	System
Period (days)			$7.047106^{\text{a}} \pm 0.000018$
Time of periastron passage, T (BJD-2400000)			$54958.791621 \pm 0.000010$
Mass ratio $q = M_2/M_1^{\text{b}}$			0.939 ± 0.075
Orbital eccentricity, e			0.600 ± 0.005
Argument of periastron, ω_p (degree)			293.0 ± 1.0
γ velocity ^b (km s^{-1})			-15.7 ± 1.7
Orbital inclination (degree), i			73.42 ± 0.27
Semi-major axis (R_{\odot}), a			23.64 ± 0.95
Mass (M_{\odot})	1.84 ± 0.18	1.73 ± 0.17	
Radius (R_{\odot})	2.01 ± 0.09	1.68 ± 0.08	
Relative radius, R/a	0.085 ± 0.002	0.071 ± 0.002	
Gravity brightening, β	0.25^{a}	0.25^{a}	
Bolometric albedo	1.0^{a}	1.0^{a}	
T_{eff} (K)	8000^{a}	8177 ± 30	
$\log g$ (cgs)	4.10 ± 0.06	4.23 ± 0.06	
pseudo-synchronous $v \sin i$ (km s^{-1})	56.4 ± 1.4	47.0 ± 1.1	
Velocity semiamplitude K^{b} (km s^{-1})	98.5 ± 5.4	104.9 ± 6.1	

^aFixed.

^bAdopted from Smullen & Kobulnicky (2015).

Table 3. Main Oscillation Frequencies of KIC 3230227

	Frequency (d^{-1})	Amplitude (10^{-3}mag)	Phase (2π)	S/N	Comment
f_1	1.40214 ± 0.00002	0.179 ± 0.027	0.97 ± 0.07	11.01	$9.88f_{orb}$
f_2	1.71988 ± 0.00002	0.192 ± 0.022	0.34 ± 0.05	14.92	$12.12f_{orb}$
f_3	1.84482 ± 0.00002	0.096 ± 0.021	0.32 ± 0.10	7.95	$13f_{orb}$
f_4	1.969765 ± 0.000008	0.338 ± 0.020	0.16 ± 0.03	29.33	$13.88f_{orb}$
f_5	2.12855 ± 0.00001	0.188 ± 0.018	0.89 ± 0.05	17.47	$15f_{orb}$
f_6	2.41235 ± 0.00001	0.189 ± 0.016	0.39 ± 0.04	20.28	$17f_{orb}$
f_7	2.55425 ± 0.00002	0.118 ± 0.015	0.85 ± 0.06	13.55	$18f_{orb}$
f_8	2.69615 ± 0.00002	0.159 ± 0.014	0.37 ± 0.04	19.84	$19f_{orb}$
f_9	2.83805 ± 0.00002	0.076 ± 0.013	0.37 ± 0.08	10.18	$20f_{orb}$
f_{10}	2.979948 ± 0.000008	0.192 ± 0.012	0.86 ± 0.03	27.52	$21f_{orb}$

Table 4. Amplitude Variations of the Main Frequencies (10^{-3} mag)

Quarter	f_1	f_2	f_3	f_4	f_5	f_6	f_7	f_8	f_9	f_{10}
Q1	0.178	0.177	0.174	0.294	0.201	0.200	0.116	0.163	0.074	0.212
Q2	0.177	0.185	0.126	0.336	0.232	0.192	0.159	0.161	0.085	0.215
Q3	0.177	0.173	0.157	0.320	0.215	0.190	0.155	0.159	0.082	0.213
Q4	0.163	0.202	0.122	0.330	0.215	0.191	0.132	0.165	0.074	0.206
Q5	0.171	0.175	0.119	0.332	0.231	0.171	0.120	0.166	0.076	0.208
Q6	0.178	0.182	0.122	0.319	0.202	0.1881	0.126	0.164	0.075	0.209
Q7	0.168	0.190	0.094	0.334	0.232	0.182	0.133	0.164	0.077	0.205
Q8	0.172	0.194	0.113	0.319	0.201	0.173	0.121	0.146	0.076	0.205
Q9	0.164	0.189	0.054	0.331	0.218	0.191	0.145	0.157	0.081	0.211
Q10	0.168	0.176	0.073	0.335	0.198	0.193	0.126	0.160	0.070	0.205
Q11	0.160	0.190	0.056	0.333	0.207	0.190	0.129	0.164	0.071	0.213
Q12	0.154	0.203	0.069	0.328	0.227	0.174	0.145	0.155	0.064	0.205
Q13	0.157	0.198	0.061	0.346	0.211	0.191	0.134	0.164	0.081	0.208
Q14	0.178	0.205	0.053	0.331	0.207	0.183	0.134	0.158	0.080	0.203
Q15	0.165	0.190	0.091	0.321	0.193	0.190	0.137	0.157	0.080	0.209
Q16	0.151	0.205	0.078	0.321	0.198	0.184	0.118	0.152	0.075	0.199
1σ error	0.027	0.022	0.021	0.020	0.018	0.015	0.015	0.014	0.013	0.012

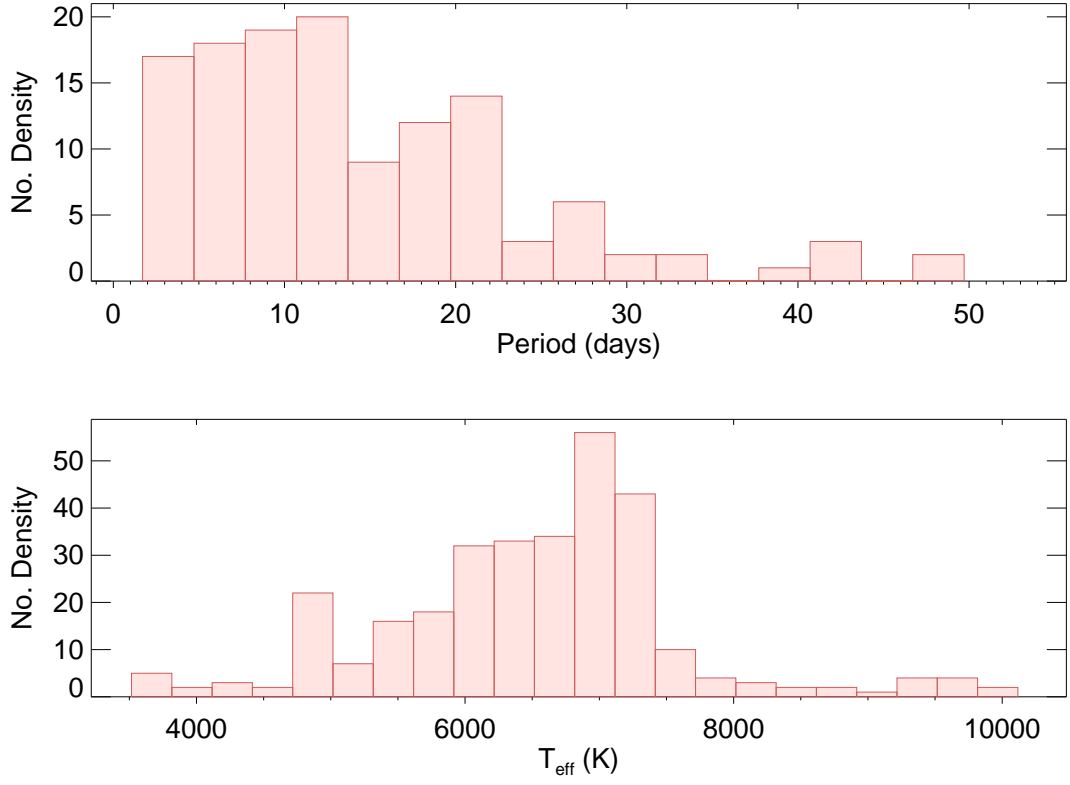


Fig. 1.— Number distribution of orbital period (upper panel) and effective temperature (lower panel) for 157 HBs in *Kepler* eclipsing binary catalog.

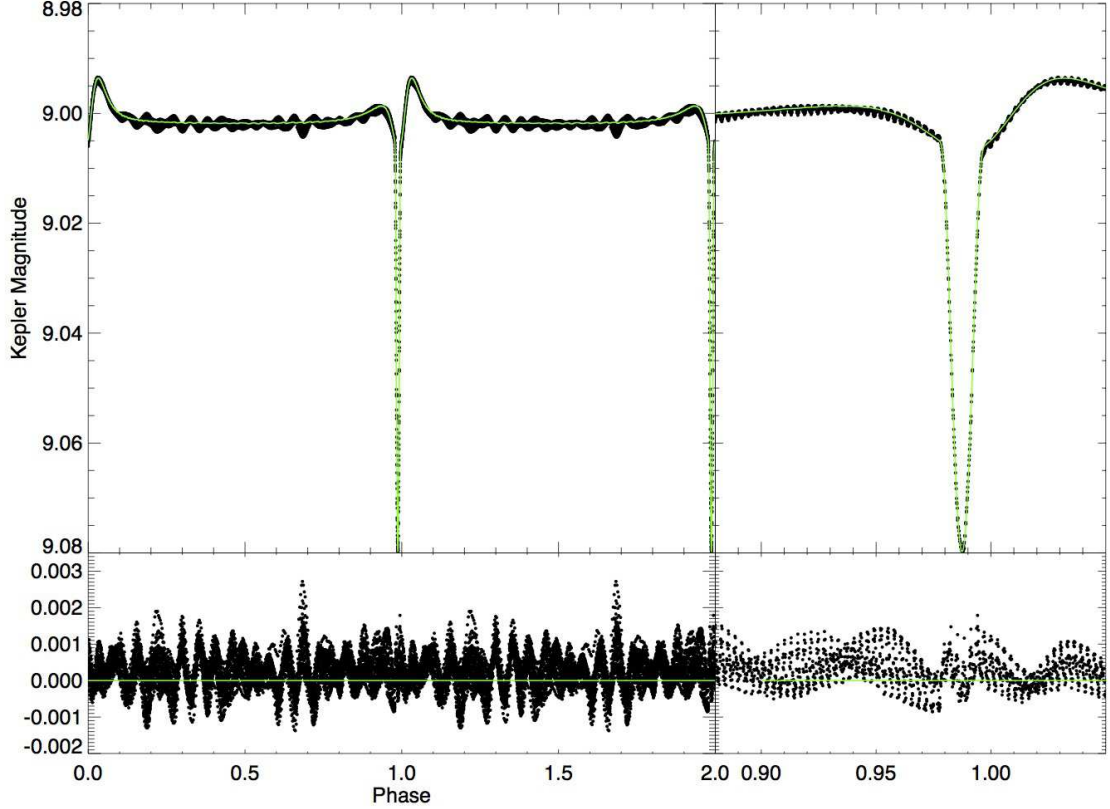


Fig. 2.— The phase-folded long cadence light curve of KIC 3230227 (dots) in Quarter 5 and 6 and the best model from ELC (green solid line). The right panel shows the light curve around the eclipses, and the bottom panels show the corresponding residuals. Note that the seemingly high-frequency ‘oscillations’ in the upper-right panel are artifacts of folding the long cadence data and are not real. This is confirmed by the absence of high-frequency peaks in the Fourier spectrum of short cadence light curves.

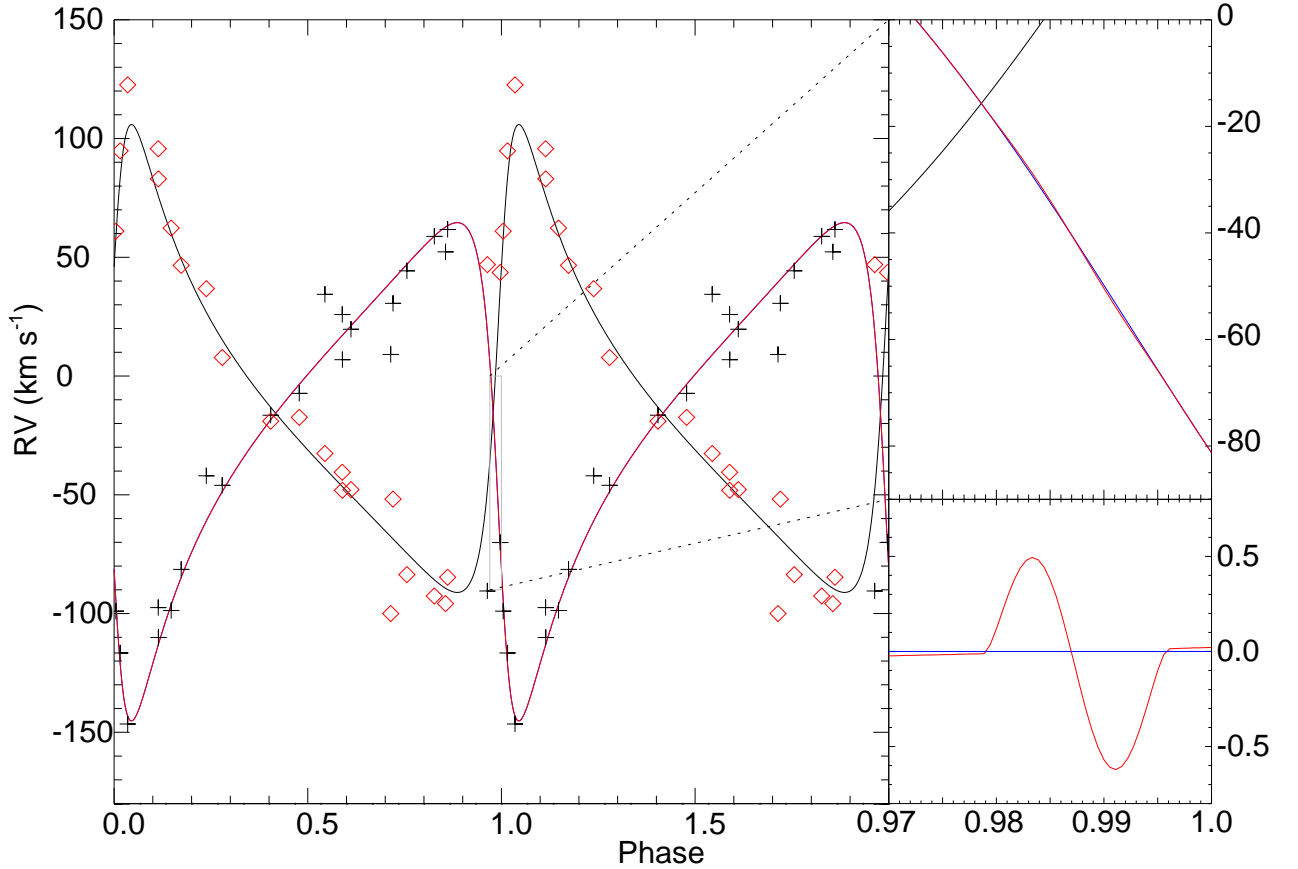


Fig. 3.— The radial velocity models of the primary (black solid) and the secondary (red solid) star from ELC. The periastron passage corresponds to phase zero. The corresponding observed radial velocities are indicated as red diamonds and black crosses. The upper right panels shows the RVs during the eclipse. The red curve represents a flux-weighted radial velocity model and blue curve is a simple Keplerian model. The RV residuals of the two models are shown in the lower right panel.

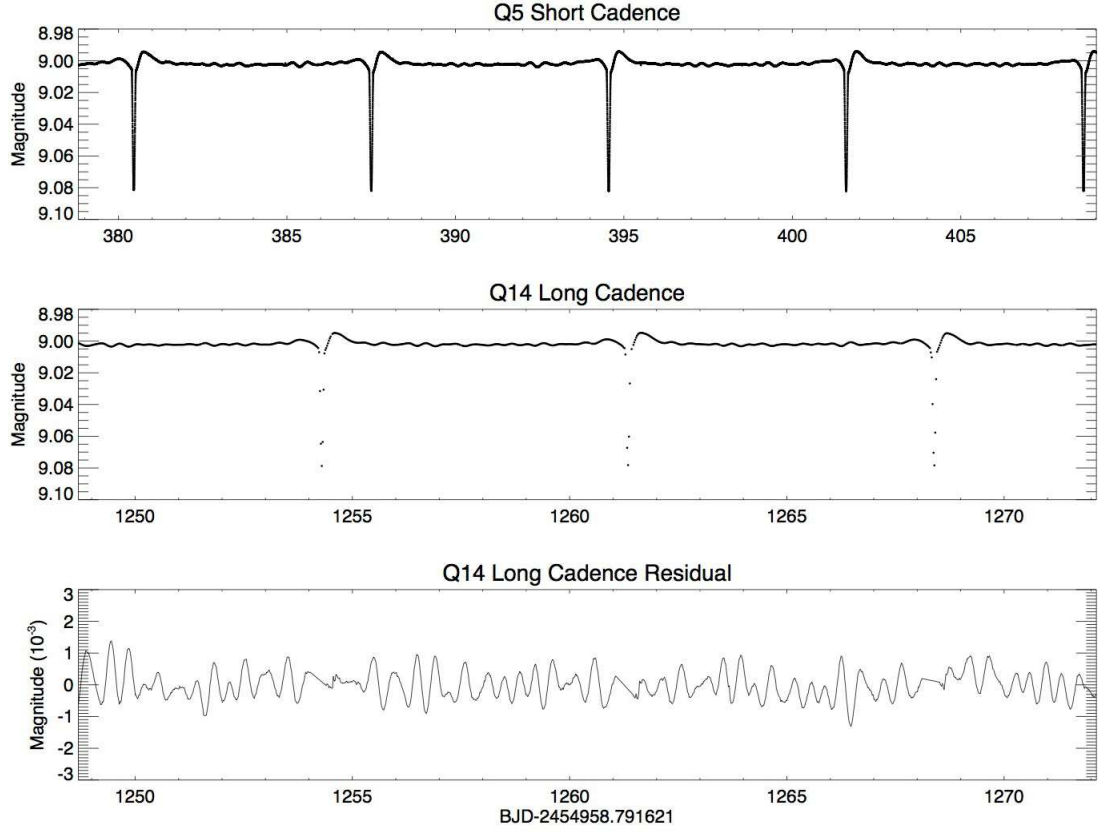


Fig. 4.— **Upper panel:** The short cadence light curve in quarter 5. **Middle panel:** The long cadence light curve in quarter 14. **Lower panel:** The light curve residuals after subtracting the best-fit binary light curve model in quarter 14. Eclipses have been masked.

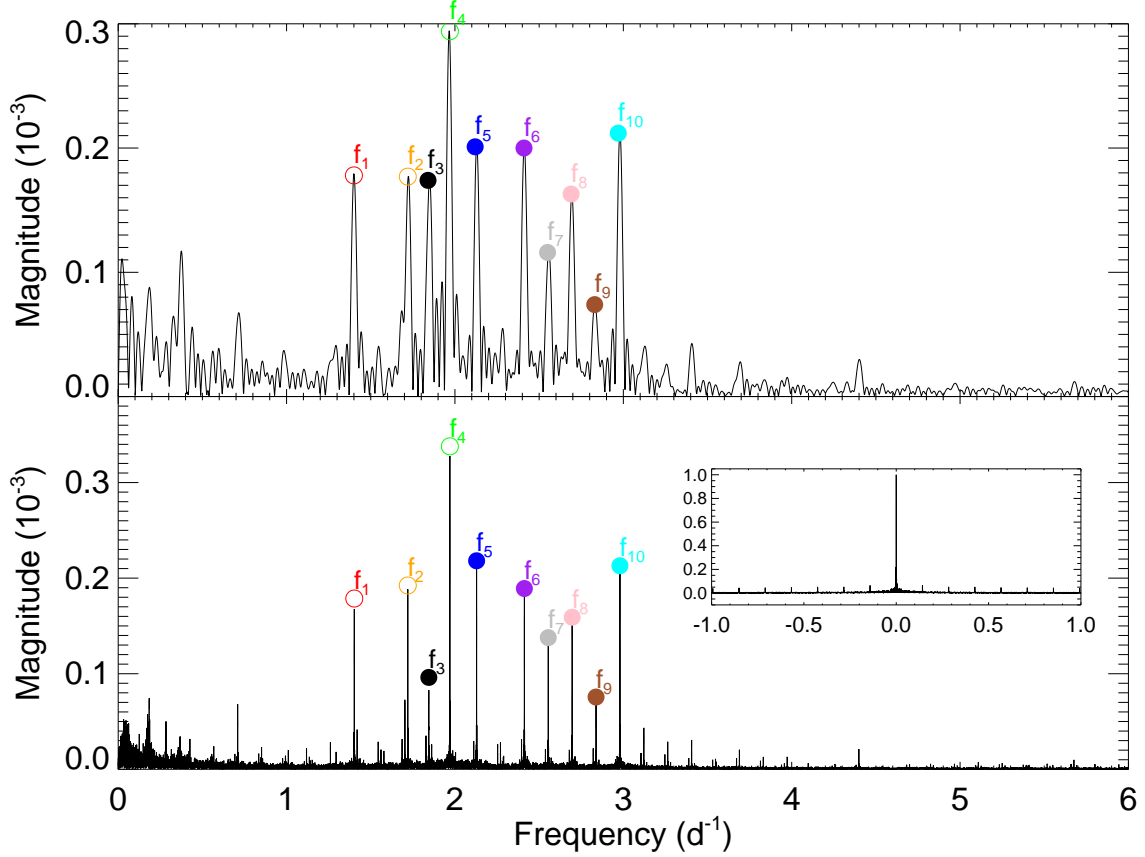


Fig. 5.— Fourier spectrum of light curve residuals with eclipses masked. The upper panel was calculated from the quarter 1 long cadence data. The lower panel presents a similar plot but using all quarters (Q0 – 17) of long cadence data. The 10 dominant frequencies listed in Table 2 are labeled. Filled and open circles mark the harmonic and nonharmonic orbital frequencies, respectively. The spectral window is shown in the inset.

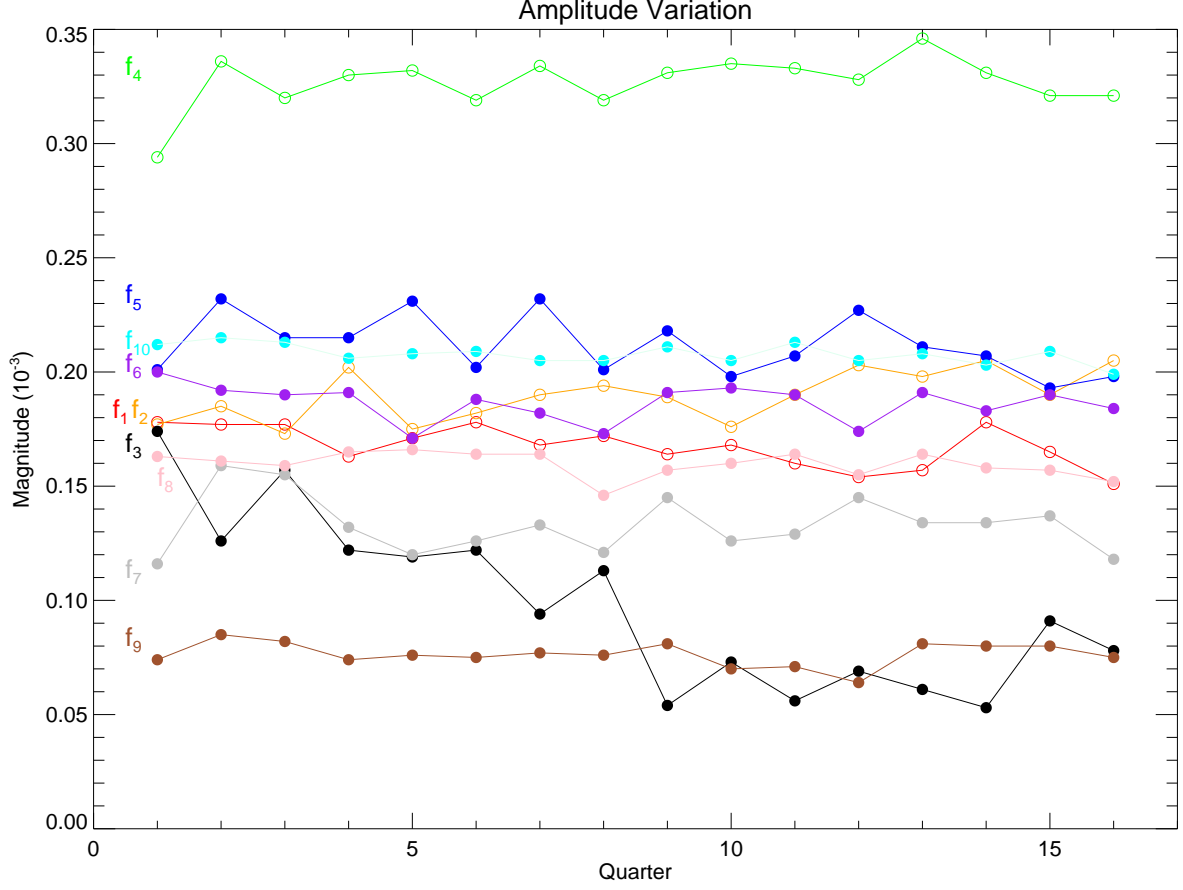


Fig. 6.— The amplitude variations of ten dominant oscillation frequencies (Table 3 and 4). Filled and open circles indicate the harmonic and nonharmonic orbital frequencies, respectively.

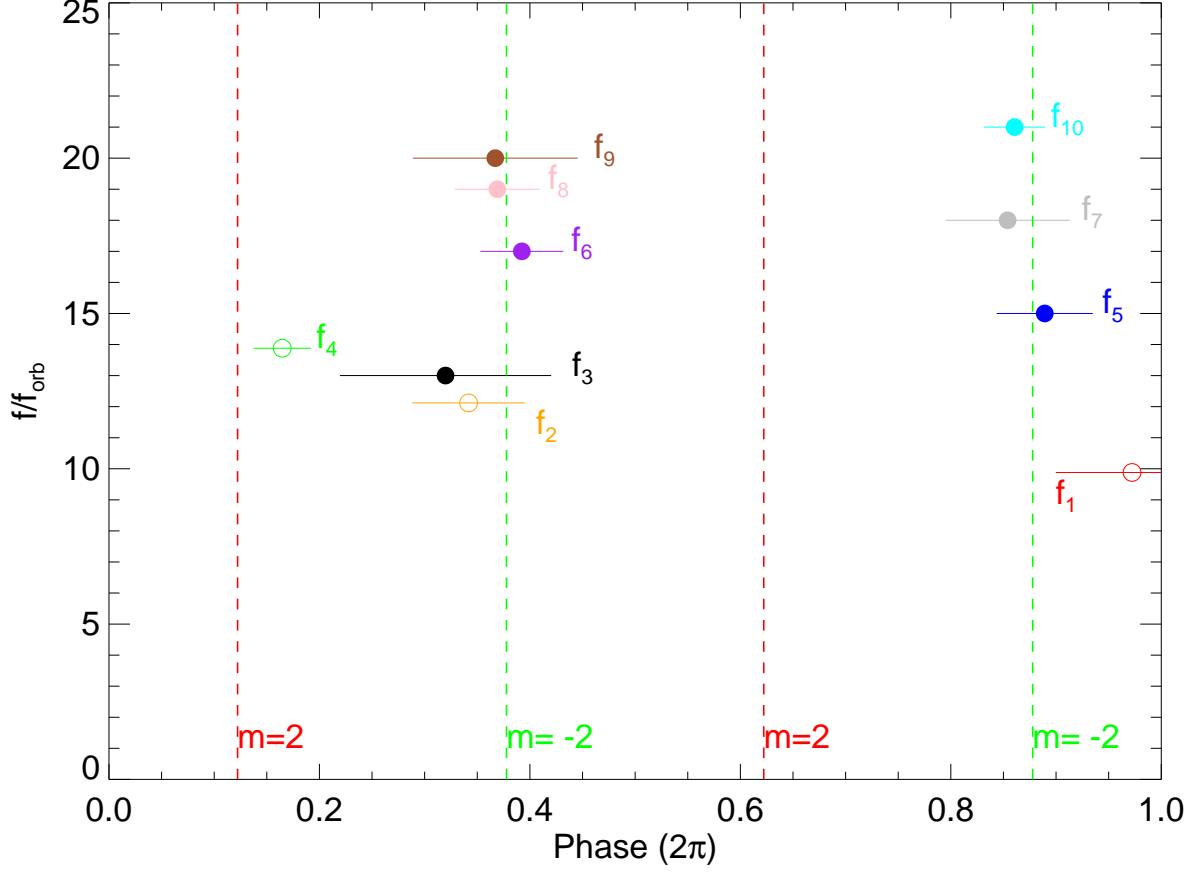


Fig. 7.— Phases of ten dominant oscillations (see Table 3). The 1σ error bars of phases are shown, and those of frequencies are smaller than the symbols. Red and green dotted lines indicate the theoretical phases of $l = 2, m = 2$ and $l = 2, m = -2$ modes. Filled and open circles indicate the harmonic and nonharmonic orbital frequencies, respectively.

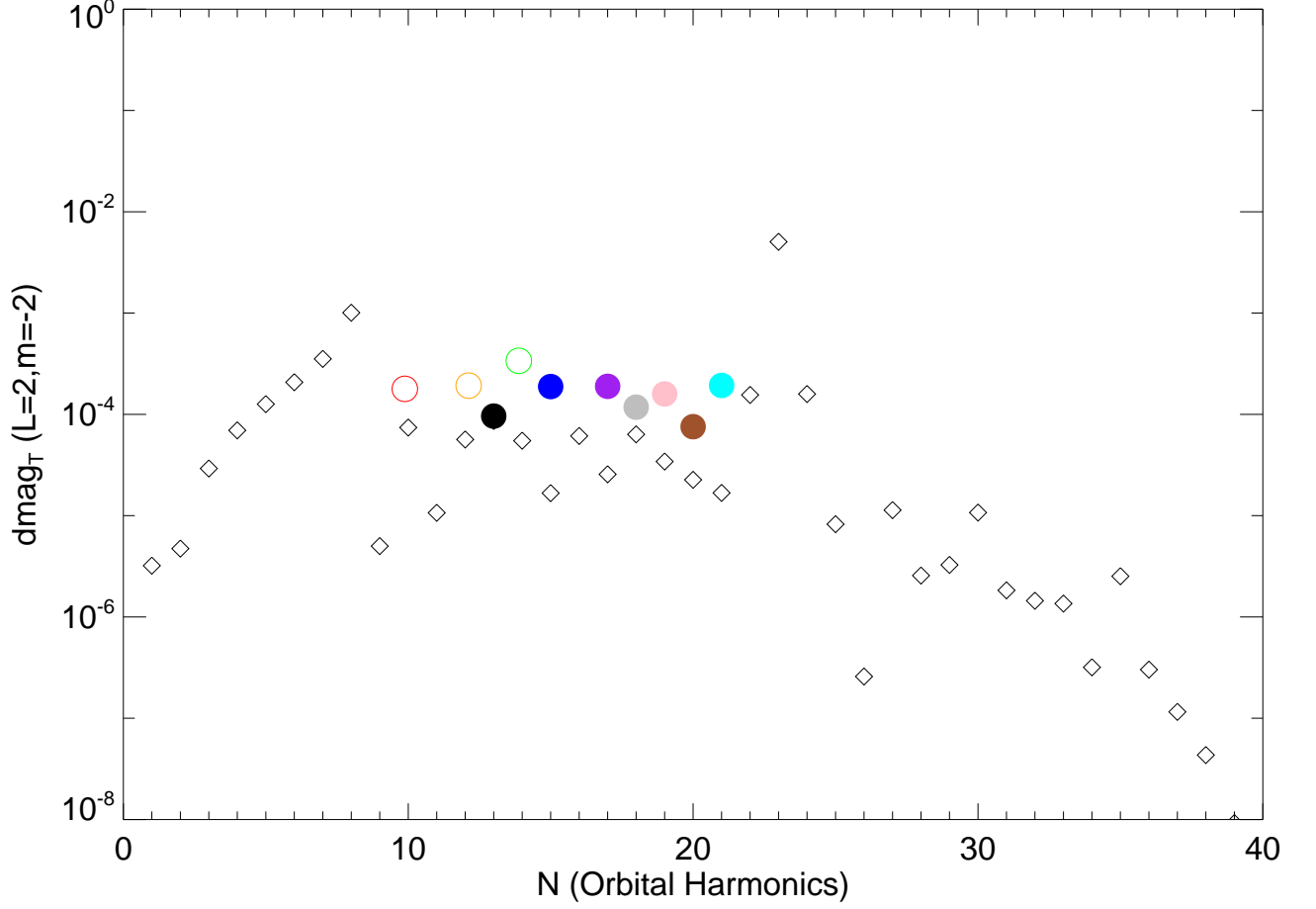


Fig. 8.— Theoretical magnitude variations of $l = 2, m = -2$ prograde modes are indicated by diamonds. The observed magnitudes of oscillations are shown as color symbols. Oscillation frequencies that are orbital harmonics are indicated by the filled circles, and otherwise by open circles.